Supporting Information

Manganese Buffer Induced High-performance Disordered MnVO Cathodes in Zinc Battery

Shiqiang Wei[a,†], Shuangming Chen[a,†], Xiaozhi Su[b], Zhenghang Qi[a], Changda Wang[a], Babu Ganguli[d], Pengjun Zhang[a], Kefu Zhu[a], Yuyang Cao[a], Qun He[a], Dengfeng Cao[a], Xin Guo[a], Wen Wen[b], Xiaojun Wu[c], Pulickel M. Ajayan[d] and Li Song[a]*

[a] National Synchrotron Radiation Laboratory, CAS Center for Excellence in Nanoscience, University of Science and Technology of China, Hefei, Anhui 230029, P.R. China.

[b] Shanghai Synchrotron Radiation Facility, Shanghai Advanced Research Institute, Chinese Academy of Sciences, Shanghai 201204, P.R. China.

[c] School of Chemistry and Material Sciences, University of Science and Technology of China, Hefei, Anhui 230026, P.R. China.

[d] Department of Materials Science and Nano Engineering, Rice University, Houston, TX 77005, USA.

Email: song2012@ustc.edu.cn

† These authors contributed equally to this work.

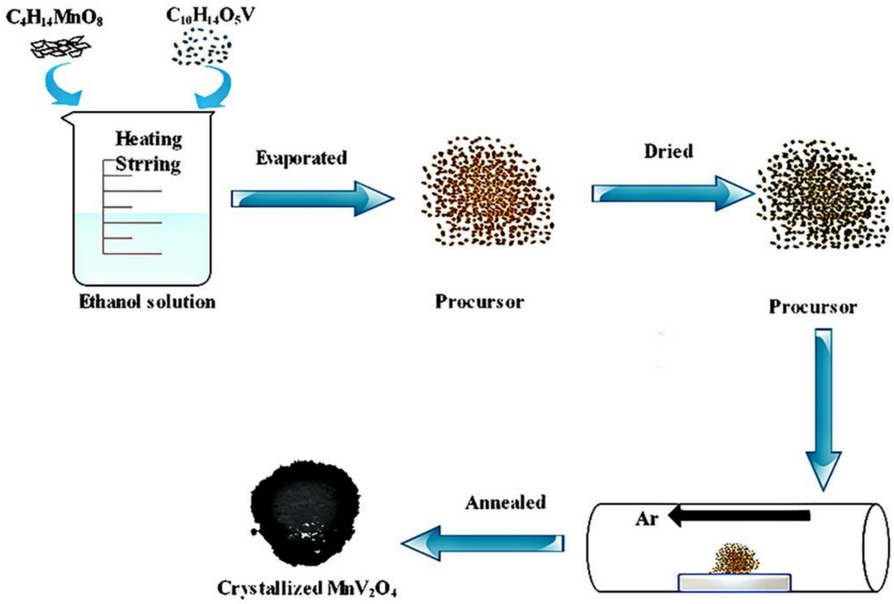

Figure S1. Diagrammatic sketch of synthesis process for MnVO spinel sample. The preparation process of MnVO model sample, or MnVO@C sample, mainly includes two steps: (1) Acquisition of precursors through evaporation and desiccation; (2) Crystallization through high temperature calcination. See the Methods section for more detail.

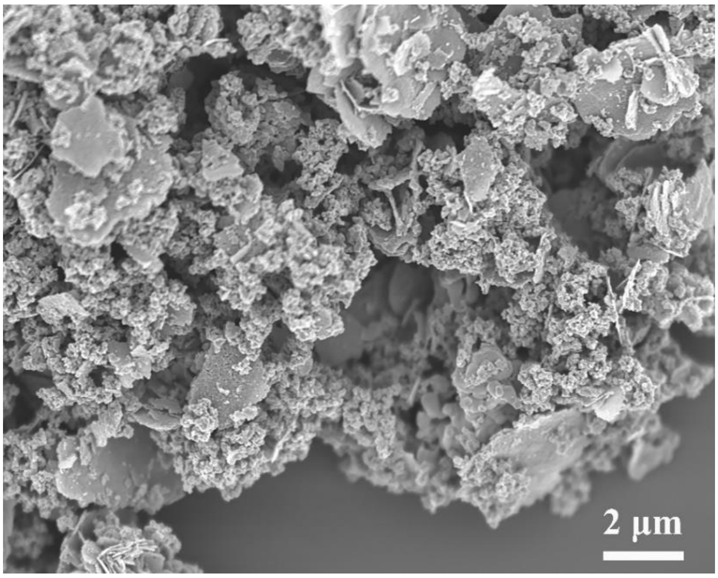

Figure S2. Scanning electron microscope (SEM) image of MnVO spinel. The morphology of MnVO sample is micron-nano-sized particles, which assure the full contact of active material and electrolyte. These particles have the same traditional morphology as other spinels synthesized by high temperature calcination, like spinels for lithium ion battery (LIB) and spinels for zinc ion battery (ZIB).[1, 2]

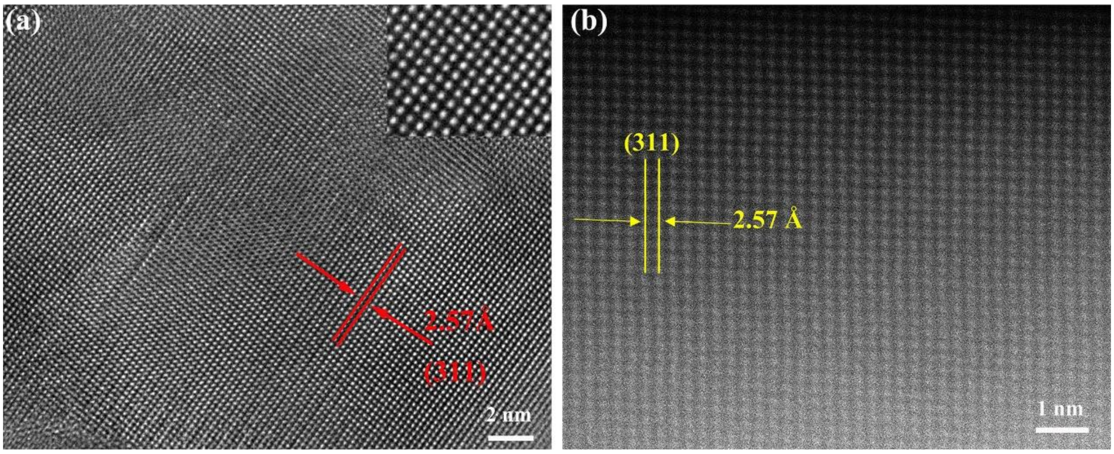

Figure S3. Transmission electron microscope. (a) High resolution transmission electron microscope (HR-TEM) image of MnVO spinel, inset is the magnification of local image. It is clearly shown that the well crystallized and orderly structure can be obtained. The high crystallinity is attributed to the high temperature of 800 ℃ used in annealed process. The crystalline interplanar spacing of 2.57 Å is indexed to crystallographic planes of (311) of MnVO spinel, indicating the successful preparation for structure model. (b) Atomic resolution HAADF-STEM image of MnVO spinel. The features of high crystallization and free of defects for MnVO spinel are further shown in atomic resolution STEM image.

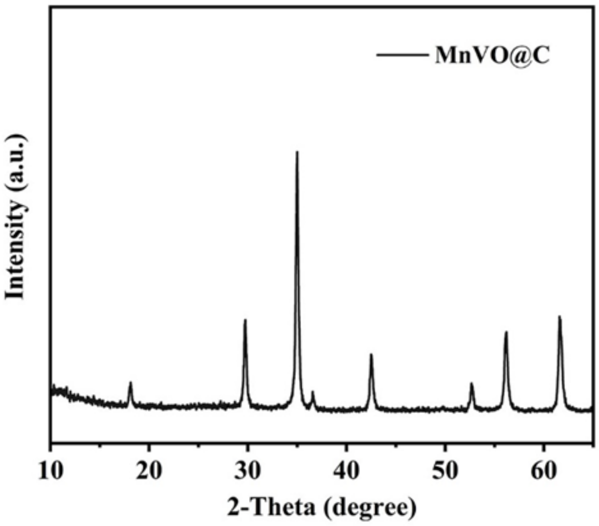

Figure S4. X-ray diffraction (XRD) curve of MnVO@C spinel. The carbon-coated sample of MnVO@C shows identical diffraction peaks to MnVO, indicating the amorphous nature of coated carbon. Amorphous materials, with more active sites, high conductivity and structure stability, are regarded to benefit electrochemistry active for ions storage.[3]

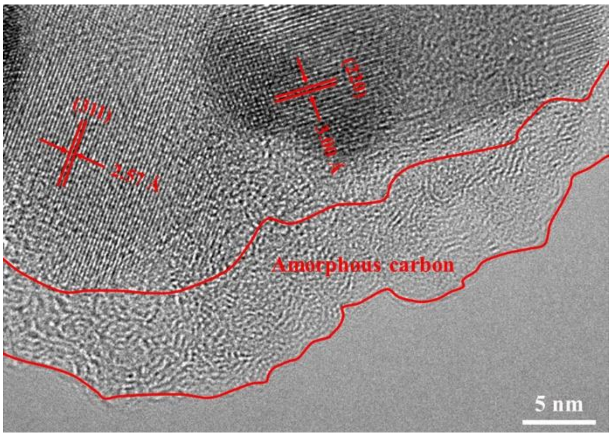

Figure S5. High resolution transmission electron microscope (HR-TEM) image of MnVO@C spinel. It is clearly shown that the amorphous carbon layer with a thickness of about 6 nm is coated on the surface of MnVO uniformly. Besides, crystallographic planes with 2.57 Å and 3.00 Å interplanar spacing correspond to (311) and (220) of MnVO, respectively.

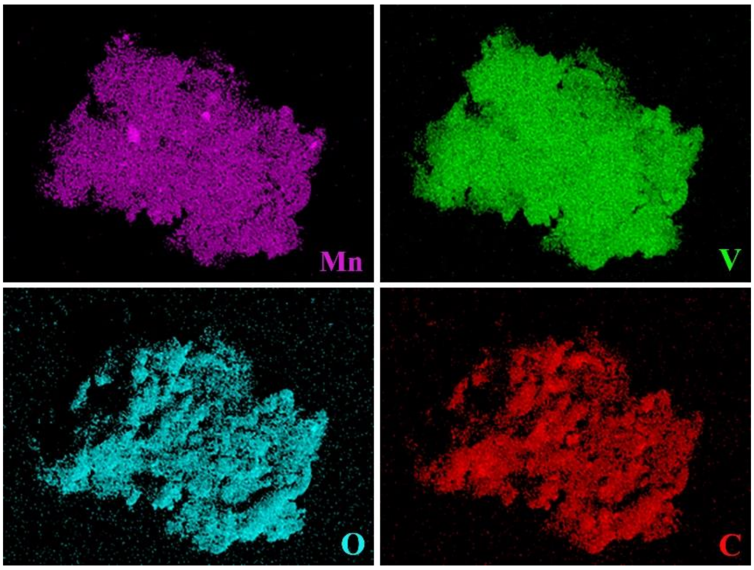

Figure S6. SEM element mapping of MnVO@C spinel. The elements of Mn, V, O and C are homogeneously dispersed in the entire area of MnVO@C. In the method for preparation of samples, the homogeneous precursor can be successfully obtained by using the liquid phase method under rapid agitation. High quality samples gauged by XRD originate in the uniformity of precursor.

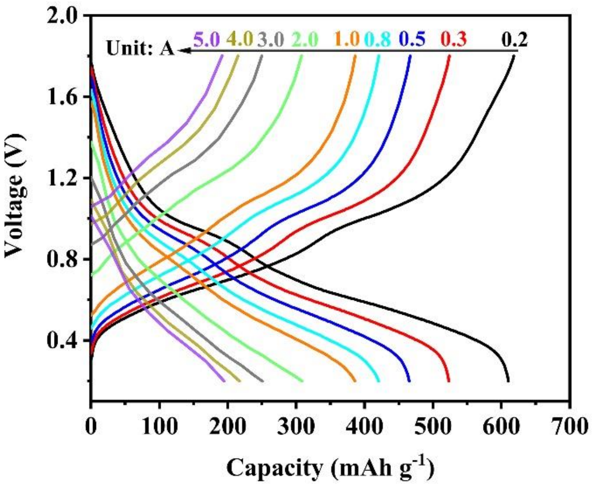

Figure S7. Galvanostatic charge-discharge (GCD) curves at different current densities for MnVO@C. After structure self-optimization, the specific capacity of MnVO@C is 610.2 mAh g^{-1} at 200 mA g^{-1} (the 10th cycle). Even at a greatly high current density of 5000 mA g^{-1}, the specific capacity still has 200 mAh g^{-1}.

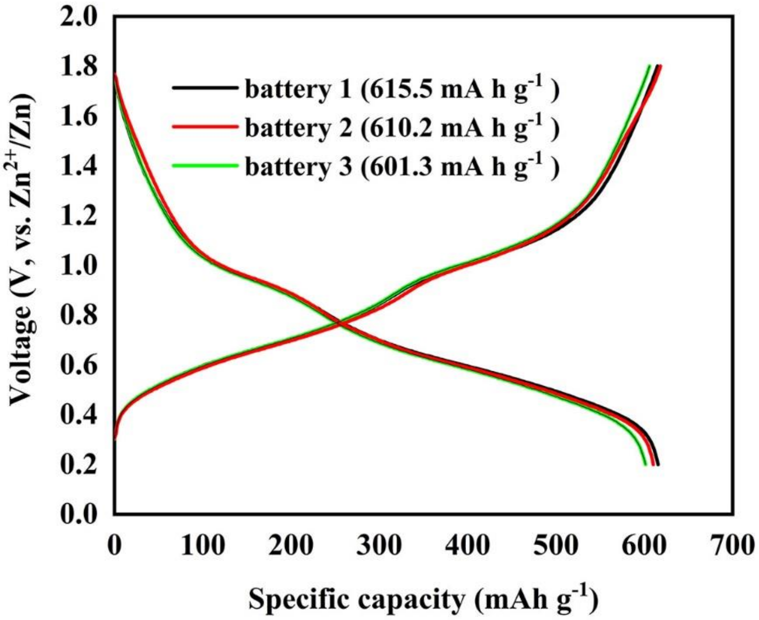

Figure S8. Specific discharged capacities of three batteries at the 10th cycles for MnVO@C. Three batteries were assembled to assess the capacity undulations. It can be seen that the battery 1, 2 and 3 have specific capacities of 615.5, 610.2 and 601.3 mAh g^{-1}, respectively. We chose the median value of 610.2 mAh g^{-1} as the representative capacity value in the main text. The average specific capacity is 609.0 mAh g^{-1} with a standard deviation of 5.86. Besides, the Coulombic efficiency of these three batteries is100.10%, 98.71% and 99.24%, respectively. The average Coulombic efficiency is 99.35% with a standard deviation of 0.99%.

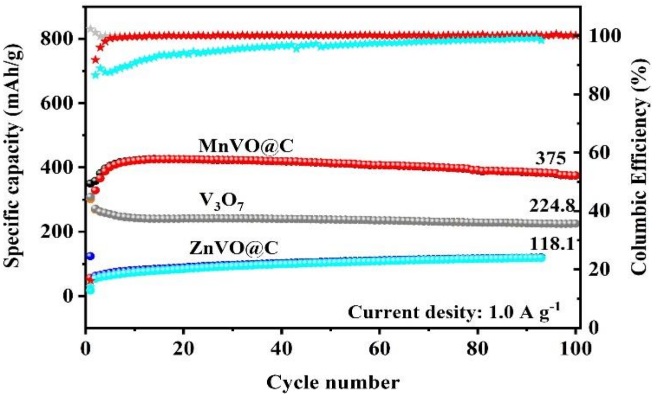

Figure S9. Cyclic stability at low current density of 1.0 A g^{-1} for MnVO@C, ZnVO@C, and V_3O_7. The cyclic stability of MnVO@C electrode at low current density was measured at 1.0 A g^{-1}. The MnVO@C electrode exhibits stable cycling with a high specific capacity of 370 mAh g^{-1} after 100 cycles, contrasting sharply with the ZnVO@C electrode and V_3O_7 electrodes without manganese (only 118.1 mAh g^{-1} for ZnVO@C and 224.8 mAh g^{-1} after 100 cycles).

Table S1. The comparision of specific capacity between MnVO@C and other cathodes. The recent preeminent scientific reseaches on Zn ion batteries (ZIBs) are selected to compare with this work, including V-based, Mn-based oxide and other compounds. Attentively, the current density and electrolyte used in these works are noted in the table.

Serial number	Cathode	capacity (mA h g^{-1})	Current (mA g^{-1})	Electrolyte
1	$Na_{0.33}V_2O_5$[4]	367.1	100	3M $Zn(CF_3SO_3)_2$
2	V_2O_5[5]	470	200	3M $Zn(CF_3SO_3)_2$
3	$Mg_xV_2O_5{\cdot}nH_2O$[6]	353	100	3M $Zn(CF_3SO_3)_2$
4	$V_2O_5{\cdot}nH_2O$[7]	381	300	3M $Zn(CF_3SO_3)_2$
5	MnVO[8]	415	50	3M $Zn(CF_3SO_3)_2$
6	CaVO[9]	466	100	3M $Zn(CF_3SO_3)_2$
1	$K_{0.8}Mn_8O_{16}$[10]	320	100	2 M $ZnSO_4$/0.1 M $MnSO_4$
2	α-MnO_2[11]	290	90	2 M $ZnSO_4$/0.2 M $MnSO_4$
3	MGS[12]	362.2	300	2 M $ZnSO_4$/0.2 M $MnSO_4$
4	O_d-MnO_2[13]	345	200	1 M $ZnSO_4$/0.2 M $MnSO_4$
5	P-MnO_{2-x}[14]	302.8	500	2 M $ZnSO_4$/0.2 M $MnSO_4$
6	cw-MnO_2[15]	350	100	1 M $ZnSO_4$
1	VS_2[16]	190.3	50	1 M $ZnSO_4$
2	$CoFe(CN)_6$[17]	173.4	300	4 m Zn(OTf)2
3	$ZnMn_2O_4$/C[1]	150	50	3M $Zn(CF_3SO_3)_2$
4	MgV_2O_4[18]	272	200	2 M $Zn(TFSI)_2$
5	$Na_{0.14}TiS_2$[19]	140	50	2M $Zn(CF_3SO_3)_2$
6	Bi_2S_3[20]	161	200	2 M $ZnSO_4$
This work	MnVO@C	615	200	3M $Zn(CF_3SO_3)_2$

Table S2. The comparison between MnVO@C and other vanadium- based cathodes using two common descriptors of specific capacity and cycle life. The performance of MnVO@C is benchmarked with the state-of-the-art ones using specific capacity and cycle life as descriptors to illustrate the significant buffer role of Mn ions in the self-optimized cathode.

Description	Cathode	Capacity (current density A g^{-1})	Cycle life (current density A g^{-1})
Mn-optimized vanadium oxide	MnVO[8]	415 (50)	2000 (4)
	MnVO-300[21]	357 (500)	1500 (10)
Other metal ions-optimized vanadium oxide	$Zn_{0.25}V_2O_5 \cdot nH_2O$[22]	300 (300)	1000 (2.4)
	$Mg_xV_2O_5 \cdot nH_2O$[6]	353 (100)	2000 (5.0)
	δ -$Ni_{0.25}V_2O_5 \cdot nH_2O$[23]	402 (0.2)	1200 (5.0)
No metal ions-optimized vanadium oxide	PVO-60[24]	400 (0.1)	1000 (10.0)
	$VN_{0.9}O_{0.15}$[25]	603 (0.12)	1800 (25C)
	$V_2O_5 \cdot nH_2O$[7]	381 (0.06)	900 (6.0)
Amorphous vanadium oxide	A-V_2O_5/G[26]	489 (0.1)	3000 (30.0)
This work	MnVO@C	615 (0.2)	4000 (5.0)

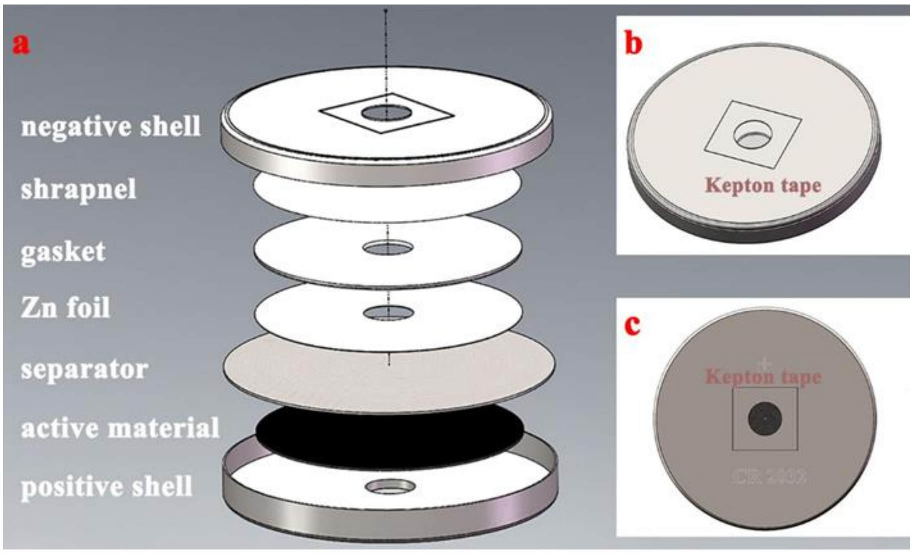

Figure S10. The diagram of hole-opening coin cell used for operando SXRD test. A hole-opening coin cell is designed based on the conventional coin cells used in laboratory. In order to pass through the X-ray, holes are punched on the center of positive shell, negative shell, gasket and Zn foil. Different from sodium and lithium, it is crucial that a hole should be bored in the center of zinc wafer in older to avert the strong adsorption of Zn for X-ray. After assembled, the holes on positive and negative shells are sealed by Kapton tapes.

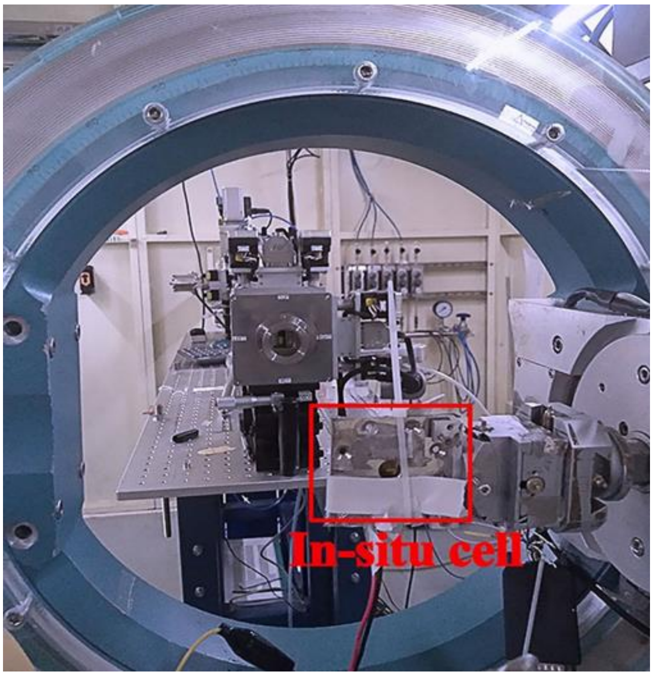

Figure S11. The measurement environment of operando SXRD test. The operando SXRD is carried on at the beamline BL14B1 in Shanghai Synchrotron Radiation Facility (SSRF), which equips with a Huber 5021 six-circle diffractometer system and a Mythen 1K linear detector. The above mentioned hole-opening coin cell (Figure S10), pasted on synchrotron radiation device, is operated on Land CT2001A battery test system.

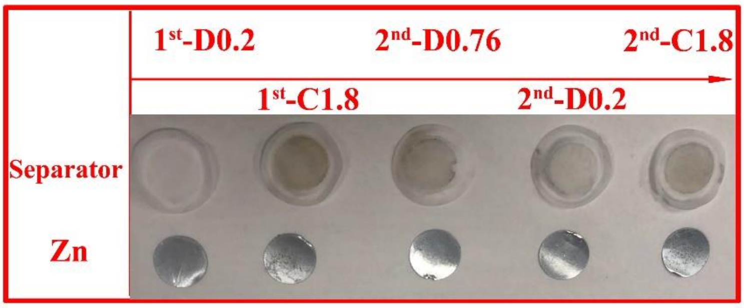

Figure S12. The separators unfolded after suffering different cut-off voltage cycles. The batteries are separated at different representative voltage states to observe what has happened inside. It is found that the separator is in white after first discharged to 0.2 V, however, the separators become darker black after first charged to 1.8 V (after structure self-optimization) and remain unchanged on subsequent cycles. The same results are also obtained for the surface of Zn anode.

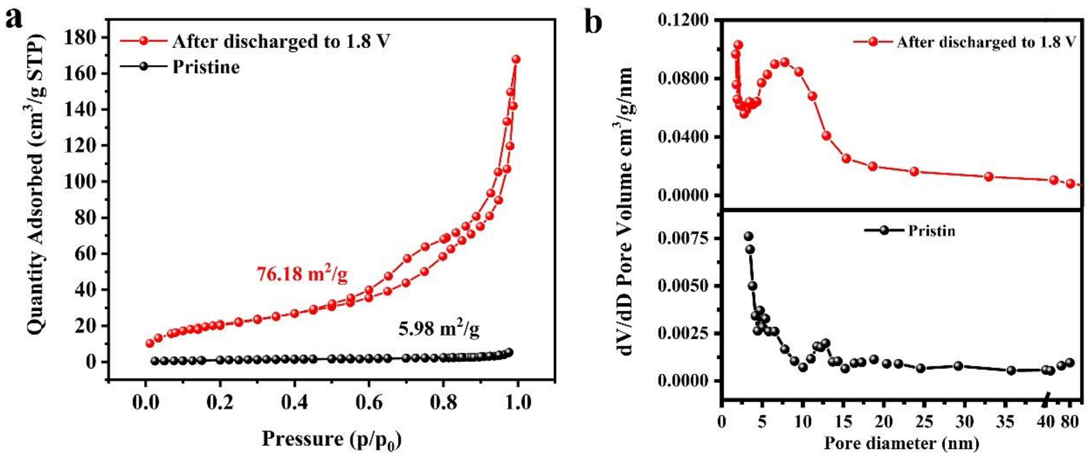

Figure S13. The specific surface area and pore size distribution of pristine MnVO@C and after charging to 1.8 V. (a) Nitrogen adsorption/desorption isotherms, (b) Pore size distribution. Notably, the specific surface area and pore size distribution analyses for pristine MnVO@C (before structure self-optimization) and after charging to 1.8 V (after structure self-optimization) show the remarkably increased specific surface area and pore volume. In detail, the specific surface area increases from 5.98 m^2 g^{-1} to 76.18 m^2 g^{-1}, which is attributed to the amorphous features of optimized electrode. The result of pore size distribution indicates that the pore diameter of optimized sample is about 10 nm that belongs to mesoporous.

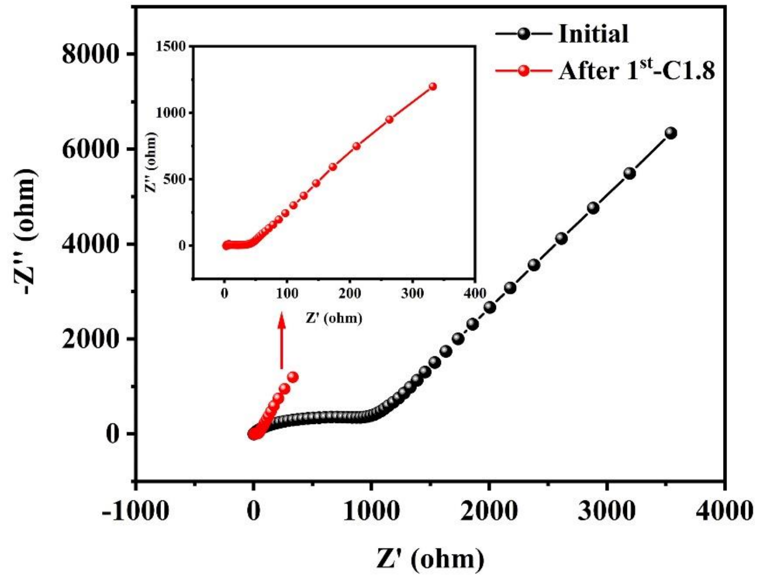

Figure S14. The electrochemical impedance spectroscopy (EIS) spectra of the MnVO@C model before (Initial) and after structure self-optimization (After 1st-C1.8). The diameter of semicircle at high frequency region represents the charge transfer resistance (R_{ct}) of the electrode/electrolyte interface. The value of R_{ct} for initial state is about 40 Ω while 1000 Ω for the state of 1st-C1.8. The rapidly descended R_{ct} is induced by structure self-optimization.

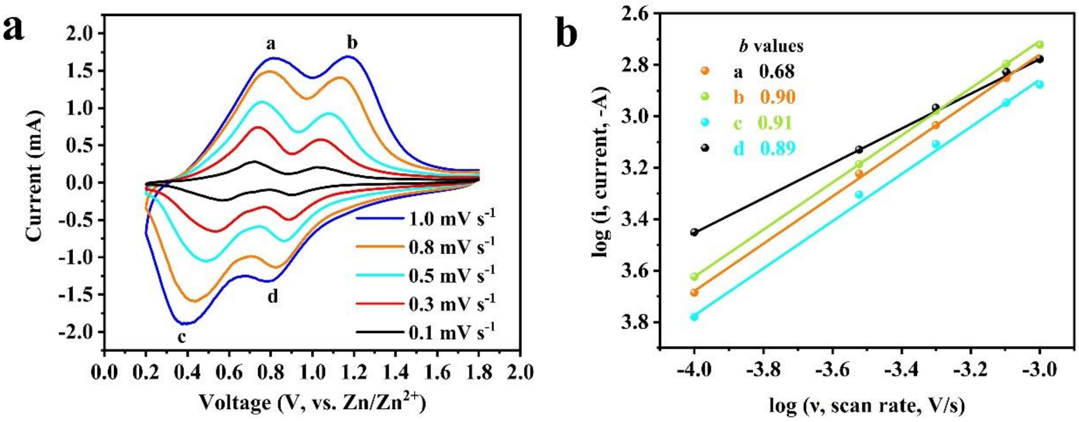

Figure S15. Kinetic analysis of Zn^{2+} for MnVO@C electrode. (a) The cyclic voltammetry (CV) curves at different scan rates. (b) The b values calculated from the CV curves. In CV, the current density i (A) and scan rate v (V/s) conform to a formula $i=av^b$, where a and b are constants. When b=0.5, it denotes a diffusion-controlled electrochemical process, and while b=1 implies a surface-controlled or capacitive electrochemical process.[27] In MnVO@C for Zn^{2+} storage, the b values calculated from peaks a, b, c and d are 0.68, 0.90, 0.91 and 0.89 respectively. It hints that the charge is stored with both diffusion-controlled and capacitance processes.

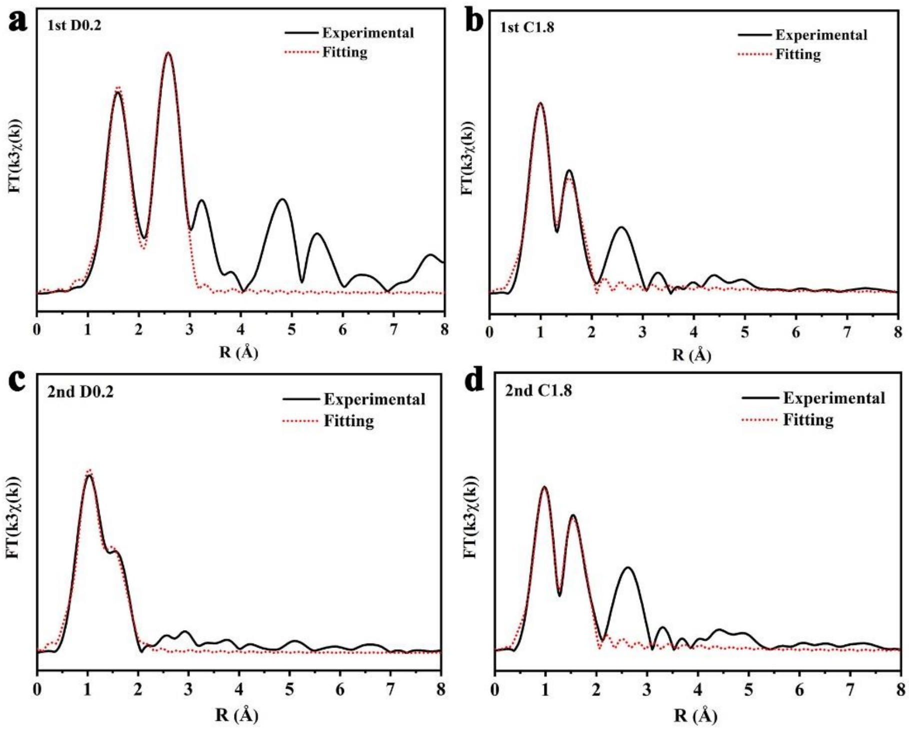

Figure S16. (a-d) V K-edge EXAFS spectra and corresponding fitting curves of MnVO@C electrodes at different states.

Table S3. V K-edge EXAFS fitting parameters.

Sample	Path	N	R (Å)	$\sigma^2(10^{-3}\ Å^2)$
1st D0.2	V-O	5.6	2.03	5.4
	V-V	6.1	3.02	6.8
1st C1.8	V-O	2.9	1.52	2.5
	V-O	1.5	1.99	2.8
2nd D0.2	V-O	3.3	1.54	2.7
	V-O	1.7	2.03	3.2
2nd C1.8	V-O	2.4	1.52	2.5
	V-O	2.3	1.98	4.9
V_2O_3	V-O	3.0*	1.93	3.2
	V-O	3.0*	2.04	2.1

N, coordination number; R, distance between absorber and backscatter atoms; σ^2, Debye-Waller factor to account for both thermal and structural disorders. Error limits (accuracies) were estimated as follows: CN, ±10%; bond length, ±1%; σ^2, ±10%. * refers to the fixed coordination number according to the standard crystal structure.

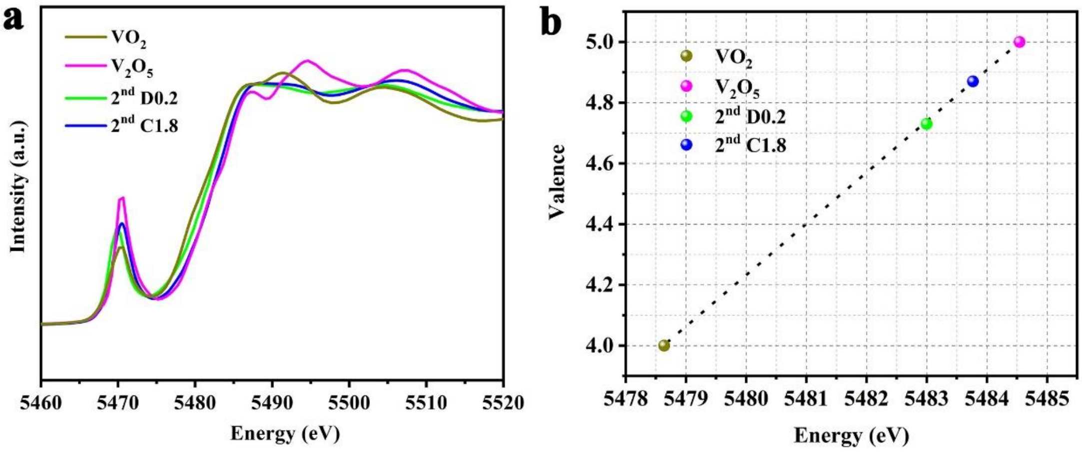

Figure S17. V K-edge XAFS study for MnVO@C electrodes. (a) The V K-edge XANES spectra of MnVO@C at various states, VO$_2$ and V$_2$O$_5$, (b) Average valence of V in VO$_2$, V$_2$O$_5$, MnVO@C electrode at 2nd D0.2 V, and 2nd C1.8 V. The energy of absorption edge is located at 5478.637 eV and 5484.542 eV for standard VO$_2$ (+4) and V$_2$O$_5$ (+5), respectively. According the linear relationship between valence and absorption energy, the average valence for MnVO@C electrode at 2nd D0.2 V (energy: 5482.998 eV) is +4.73 and for MnVO@C electrode at 2nd D0.2 V (energy: 5483.767 eV) is 4.87. Here, we got the energy of absorption edge from the position where the first-order derivative value reaches maximum.

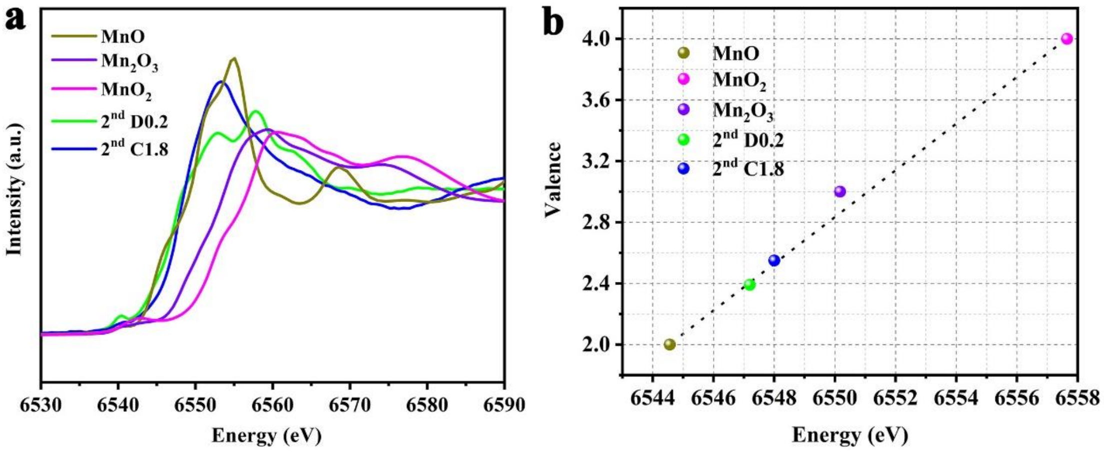

Figure S18. Mn K-edge XAFS study for MnVO@C electrodes. (a) The Mn K-edge XANES spectra of MnVO@C at various states, MnO, Mn_2O_3, MnO_2, (b) Average valence of Mn in MnO, MnO_2, Mn_2O_3, MnVO@C electrode at 1st C1.8 V, 2nd D0.2 V and 2nd C1.8 V. The energy of absorption edge is located at 6544.56 eV, 6550.17 eV and 6557.652 eV for standard MnO (+2), Mn_2O_3 (+3) and Mn_2O_5 (+4), respectively. According the linear relationship between valence and absorption energy, the average valence for MnVO@C electrode at 2nd D0.2 V (energy: 6547.197 eV) is +2.39 and for MnVO@C electrode at 2nd D0.2 V (energy: 6548.002 eV) is 2.55. Here, we got the energy of absorption edge from the position where the first-order derivative value reaches maximum.

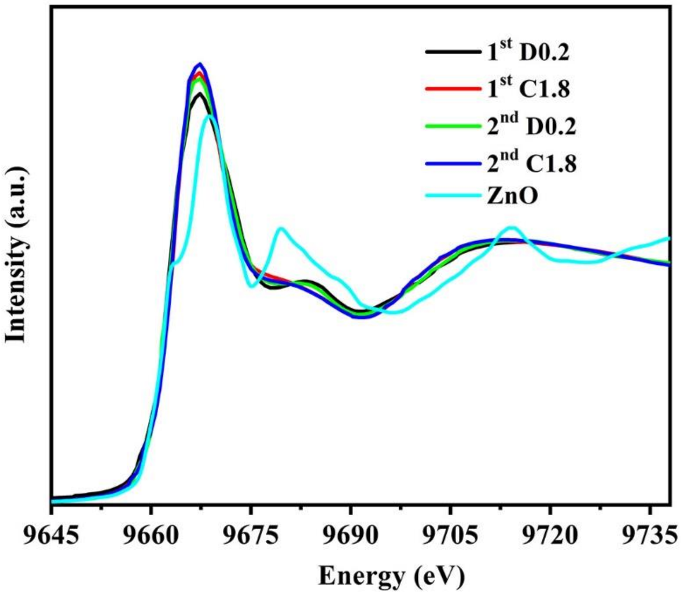

Figure S19. The Zn K-edge XANES spectra of MnVO@C at various states. There are no valence changes for Zn at any voltage states compared with the standard sample of ZnO.

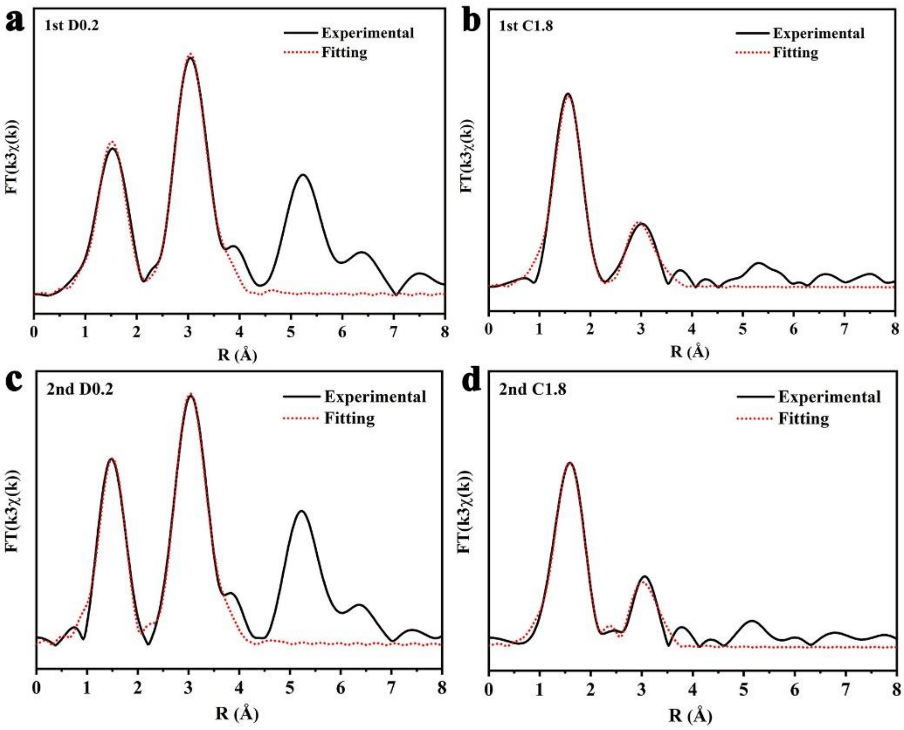

Figure S20. (a-d) Mn K-edge EXAFS spectra and corresponding fitting curves of MnVO@C electrodes at different states.

Table S4. Mn K-edge EXAFS fitting parameters.

Sample	Path	N	R (Å)	σ^2(10^{-3} Å^2)
1st D0.2	Mn-O	4.5	2.01	6.7
	Mn-V/O	11.4	3.54	6.3
	Mn-Mn	3.5	3.74	3.5
1st C1.8	Mn-O	4.9	2.08	5.2
	Mn-V/O	6.2	3.52	13.2
	Mn-Mn	0.8	3.08	5.8
2nd D0.2	Mn-O	4.4	2.00	5.7
	Mn-V/O	8.4	3.53	5.4
	Mn-Mn	3.1	3.72	3.7
2nd C1.8	Mn-O	5.0	2.09	6.4
	Mn-V/O	3.9	3.52	9.7
	Mn-Mn	2.0	3.07	14.4
MnO_2	Mn-O	3.0 *	1.84	1.8
	Mn-O	3.0 *	1.90	1.9

N, coordination number; R, distance between absorber and backscatter atoms; σ^2, Debye-Waller factor to account for both thermal and structural disorders. Error limits (accuracies) were estimated as follows: CN, ±10%; bond length, ±1%; σ^2, ±10%. * refers to the fixed coordination number according to the standard crystal structure.

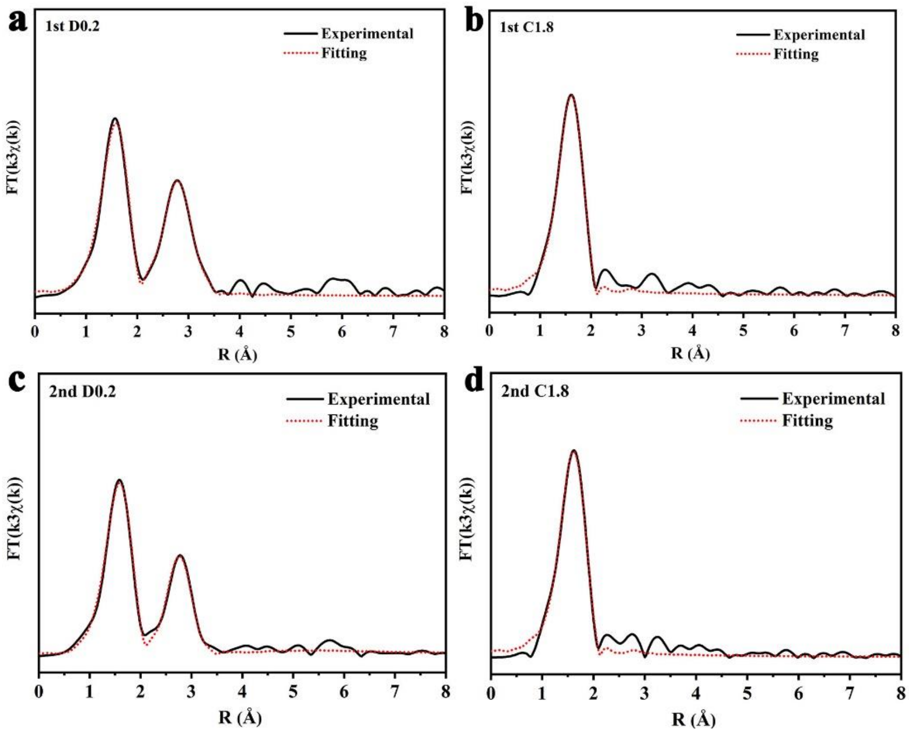

Figure S21. (a-d) Zn K-edge EXAFS spectra and corresponding fitting curves of MnVO@C electrodes at different states.

Table S5. Zn K-edge EXAFS fitting parameters.

Sample	Path	N	R (Å)	$\sigma^2(10^{-3}$ Å$^2)$
1st D0.2	Zn-O	5.9	2.02	11.3
	Zn-V	1.0	3.05	5.6
	Zn-V	3.4	3.44	9.0
1st C1.8	Zn-O	5.6	2.05	9.1
2nd D0.2	Zn-O	6.2	2.03	11.5
	Zn-V	0.8	2.92	8.1
	Zn-V	2.9	3.42	10.2
2nd C1.8	Zn-O	6.1	2.05	9.5
1 M $ZnSO_4$	Zn-O	6.0*	2.08	7.5

The different tetrahedron or octahedron cation sites are comformed by EXAFS, more precisely reflected in refinement results. Elaborately, it has been shown in the literature that the chemical bond between metal atoms in tetrahedron and oxygen ions is slightly shorter than the counterpart in octahedron ($M\text{-}O_{tetra} < M\text{-}O_{octa}$)[28, 29]. According to the refinement results in Table S4, it is finding that the length of Mn-O bond at the fully discharged (2.00 and 2.01 Å) is shorter than the bond at fully charged (2.08 and 2.09 Å). Besides, the Mn-Mn bonds at fully discharged are 3.74 and 3.72 Å, which are longer than the Mn-Mn bonds at fully charged of 3.08 and 3.07 Å, conforming to the law of the distance between two octahedron sites is commonly shorter than the bonds between two tetrahedron sites. Therefore, it can be concluded that Mn^{2+} is in tetrahedron sites when Zn^{2+} is intercalated and in octahedron sites when Zn^{2+} is extracted. Additional information can be obtained for the fitting results of Zn K-edge is the near six-coordinated environment of Zn^{2+} at the intercalated states, which indicates that the Zn^{2+} is in octahedron sites after fully discharged (Figure S21 and Table S5).

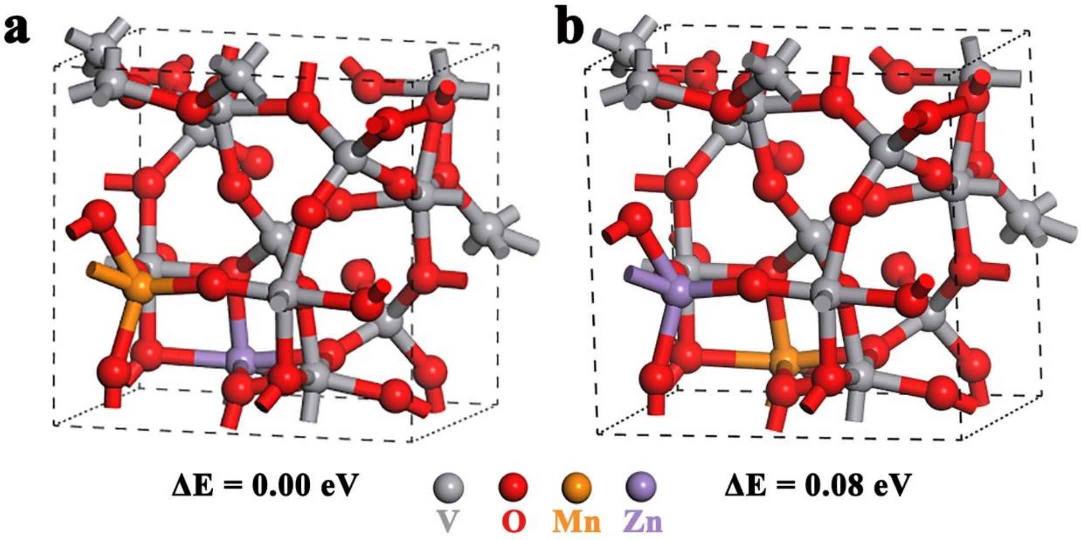

Figure S22. DFT caculation models and results. Two models of $ZnMnV_{14}O_{32}$ are set up: (a) Zn is located at the octahedral site and Mn occupies the tetrahedral site to constructure model **a** that has a calculated relative energy of 0.00eV. (b) Zn is located at the tetrahedral site and Mn occupies the octahedral site to constructure model **b** that has been proved a calculated relative energy of 0.08eV.

DFT computations were performed to further verify the competitive relationship between Zn^{2+} and Mn^{2+} for octahedral sites. Aiming to closely correlate with the experimental structure of self-optimized MnVO, two models of $ZnMnV_{14}O_{32}$ were constructed as shown in Figures S22. In the model **a** (Figure S22a), Zn is located at the octahedral site while Mn occupies the tetrahedral site. Compared to model **a**, Zn and Mn exchanged corresponding positions to construct model **b**, as shown in Figure S22b. The DFT calculation results show that the system energy of model a is 0.00 eV lower than the model b with energy 0.08 eV, relatively. The energy difference of the two models indicates that the model a is more favorable than model b with an equilibrium ratio of >95:5 at room temperature according to the Boltzmann distribution. These results of DFT computation demonstrate that Zn are more favorable to occupy the octahedral site than Mn when Zn ions are embedded, which is in good agreement with the experimental results.

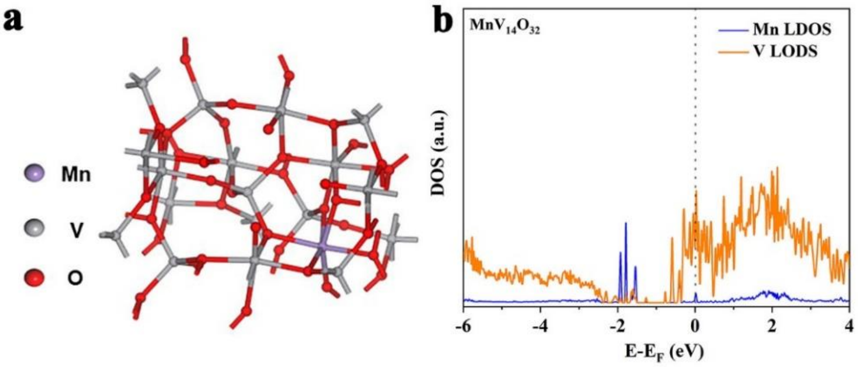

Figure S23. (a) The model of $MnV_{14}O_{32}$. (b) Local DOS of the model of $MnV_{14}O_{32}$.

To further analyze the buffer effect of Mn ions, we have constructed a $MnV_{14}O_{32}$ model that Mn ions are located at the octahedral sites as shown in Figure 23a. As shown in the local density of state (LDOS) plots of Mn and V atoms (Figure 23b), the Mn atom contributes most of the valence band, which is mostly composed of Mn 3d states. Thus, it is reasonable to consider that the Fermi surface shift is associated with the presence of Mn atoms, and in particular, with the distribution of the 3d states of Mn.

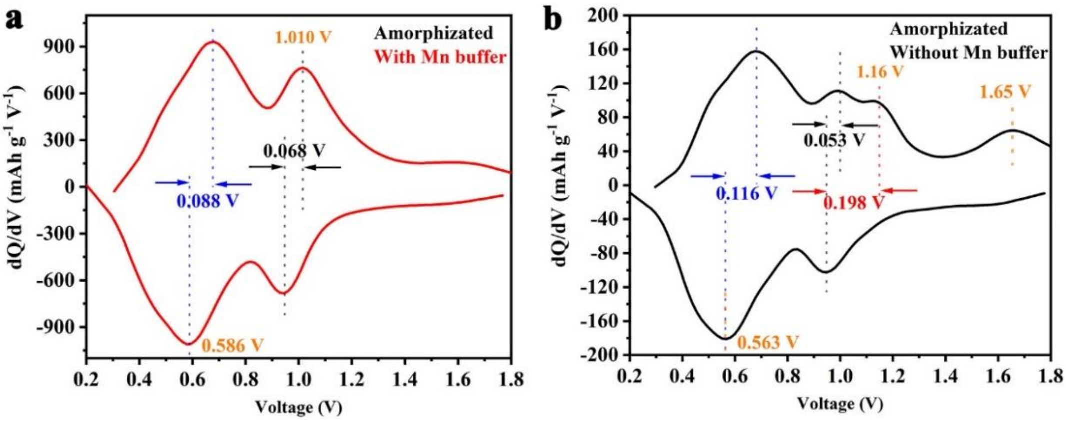

Figure S24. The dQ/dV curves at 0.2 A g^{-1} for MnVO@C electrode (a) and ZnVO@C electrode (b).

For comparison of the difference with or without Mn buffer, the electrochemical behavior during Zn^{2+} insertion and prolapse of MnVO@C and ZnVO@C is analyzed by dQ/dV curves. Two takeaways can be drawn from Figure S24: (1) **The MnVO@C electrode shows higher reduction potential and lower oxidation potential.** Specifically, the last reduction reaction of V in MnVO@C electrode happens at 0.586 V while 0.563 V for no Mn buffer one. For oxidation process, the right-most oxidation peak is at 1.01 V for MnVO@C while a new peak at 1.16 V is observed for ZnVO@C. These results indicate that in MnVO@C electrode the valence of V would not be reduced as much as ZnVO@C and equally would not be oxidized to 1.15 V like in ZnVO@C electrode as the result of Mn buffer (**voltage change become smaller**). In other words, the Fermi surface of V 3d in MnVO@C electrode would not ascend/decline as much as ZnVO@C during Zn^{2+} de/intercalated process with the help of Mn buffer. (2) **The MnVO@C electrode shows lower overpotential and polarization.** Specifically, the two coupled redox waves in MnVO@C electrode show an overpotential 0.088 and 0.068 V, respectively. For ZnVO@C electrode, the ZnVO@C electrode shows an overpotential of 0.116 V at the low voltage region, and at high voltage, the reduction peak corresponds to two oxidation peaks that with an overpotential of 0.053 and 0.198 V, respectively. Besides, an obvious polarization peak is found at 1.65 V for ZnVO@C, conversely, no polarization exists in MnVO@C at the high voltage region. Lower overpotential and free polarization would be instrumental in the stability of electrode host during Zn^{2+} de/intercalation process. In consequence, such Mn-migration not only stabilizes the main structure of vanadium-based electrode, but also modulates the Fermi surface of V 3d against overmuch drift.

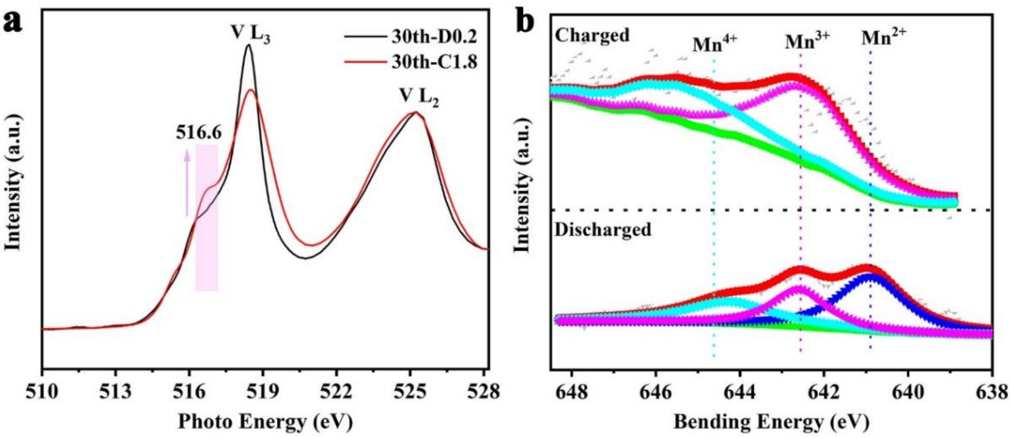

Figure S25. Research of structure evolution at the 30th cycle of MnVO@C electrode. (a) V L-edge sXAS spectra. (b) High-resolution XPS spectra of Zn.

The MnVO@C cathode at the 30th cycle evolves the same regular pattern as the 2nd cycle, which proves the consistency of its structure evolution mechanism in the following cycles. Specifically, for V soft XAS (Figure S25a), the obtained information is the structure response for Zn^{2+} insertion and extraction characterized by the peaks that occurred at 516.4 eV. According to previous studies, this peak is considered to be $2p_{3/2}$ to b_2 (d_{xy}) transition. Upon discharge, the intensity of this peak becomes much weaker, indicating the higher electron filled density compared with the charged state. Two inferences could be drawn from the XPS spectra of Mn $2p_{3/2}$ of the 30th cycle at the fully charged and discharged states (Figure S25b). First and foremost, the Mn element persists in the material host and does not dissolve into electrolyte, which pledges the permanent buffer role of manganese during cycling. Secondly, there are three valences of +2, +3 and+4 that can be observed at fully discharged state while only +3 and higher +3 are in fully charged state, indicating the valence rising in the process of charging. The existence of Mn^{3+}, Mn^{4+} at fully discharged state, and higher valence Mn at charged state may attribute to surface oxidation of Mn during washing and testing process. In brief, the variety of Mn valence further verifies the migration of tiny Mn from tetrahedral to octahedral sites (+2 to +3) during charging process.

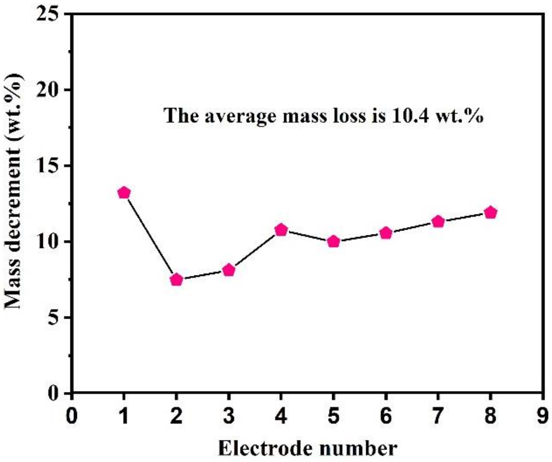

Figure S26. Mass change of MnVO@C electrode after first structure reconstruction. We measured the mass decrement after first fully charged, it is finding that the average mass lose is 10.4 wt. %. The measured mass decrement is less than the theoretical value of Mn dissolution due to the compensation of oxygen.

REFERENCES

1 N. Zhang, F. Cheng, Y. Liu, Q. Zhao, K. Lei, C. Chen, X. Liu and J. Chen, *J. Am. Chem. Soc.*, 2016, **138**, 12894-12901.

2 Y. Tao, Z. Li, L. Tang, X. Pu, T. Cao, D. Cheng, Q. Xu, H. Liu, Y. Wang and Y. Xia, *Electrochim. Acta*, 2020, **331**, 135296.

3 Y. Li, Q. Zhang, Y. Yuan, H. Liu, C. Yang, Z. Lin and J. Lu, *Adv. Energy Mater.*, 2020, **10**, 2000717.

4 P. He, G. Zhang, X. Liao, M. Yan, X. Xu, Q. An, J. Liu and L. Mai, *Adv. Energy Mater.*, 2018, **8**, 1702463.

5 N. Zhang, Y. Dong, M. Jia, X. Bian, Y. Wang, M. Qiu, J. Xu, Y. Liu, L. Jiao and F. Cheng, *ACS Energy Lett.*, 2018, **3**, 1366-1372.

6 F. Ming, H. Liang, Y. Lei, S. Kandambeth, M. Eddaoudi and H. N. Alshareef, *ACS Energy Lett.*, 2018, **3**, 2602-2609.

7 M. Yan, P. He, Y. Chen, S. Wang, Q. Wei, K. Zhao, X. Xu, Q. An, Y. Shuang, Y. Shao, K. T. Mueller, L. Mai, J. Liu and J. Yang, *Adv. Mater.*, 2018, **30**, 1703725.

8 C. Liu, Z. Neale, J. Zheng, X. Jia, J. Huang, M. Yan, M. Tian, M. Wang, J. Yang and G. Cao, *Energy Environ. Sci.*, 2019, **12**, 2273-2285.

9 K. Zhu, T. Wu and K. Huang, *ACS Nano*, 2019, **13**, 14447-14458.

10 G. Fang, C. Zhu, M. Chen, J. Zhou, B. Tang, X. Cao, X. Zheng, A. Pan and S. Liang, *Adv. Funct. Mater.*, 2019, **29**, 1808375.

11 W. Sun, F. Wang, S. Hou, C. Yang, X. Fan, Z. Ma, T. Gao, F. Han, R. Hu, M. Zhu and C. Wang, *J. Am. Chem. Soc.*, 2017, **139**, 9775-9778.

12 B. Wu, G. Zhang, M. Yan, T. Xiong, P. He, L. He, X. Xu and L. Mai, *Small*, 2018, **14**, e1703850.

13 T. Xiong, Z. G. Yu, H. Wu, Y. Du, Q. Xie, J. Chen, Y. W. Zhang, S. J. Pennycook, W. S. V. Lee and J. Xue, *Adv. Energy Mater.*, 2019, **9**, 1803815.

14 Y. Zhang, S. Deng, G. Pan, H. Zhang, B. Liu, X. L. Wang, X. Zheng, Q. Liu, X. Wang, X. Xia and J. Tu, *Small Methods*, 2020, **4**, 1900828.

15 K. W. Nam, H. Kim, J. H. Choi and J. W. Choi, *Energy Environ. Sci.*, 2019, **12**, 1999-2009.

16 P. He, M. Yan, G. Zhang, R. Sun, L. Chen, Q. An and L. Mai, *Adv. Energy Mater.*, 2017, **7**, 1601920.

17 L. Ma, S. Chen, C. Long, X. Li, Y. Zhao, Z. Liu, Z. Huang, B. Dong, J. A. Zapien and C. Zhi, *Adv. Energy Mater.*, 2019, **9**, 1902446.

18 W. Tang, B. Lan, C. Tang, Q. An, L. Chen, W. Zhang, C. Zuo, S. Dong and P. Luo, *ACS Sustain. Chem. Eng.*, 2020, **8**, 3681-3688.

19 W. Li, K. Wang, S. Cheng and K. Jiang, *Adv. Energy Mater.*, 2019, **9**, 1900993.

20 T. Xiong, Y. Wang, B. Yin, W. Shi, W. S. V. Lee and J. Xue, *Nano-Micro Lett.*, 2019, **12**, 8.

21 Y. Yang, Y. Tang, S. Liang, Z. Wu, G. Fang, X. Cao, C. Wang, T. Lin, A. Pan and J. Zhou, *Nano Energy*, 2019, **61**, 617-625.

22 D. Kundu, B. D. Adams, V. Duffort, S. H. Vajargah and L. F. Nazar, *Nat. Energy*, 2016, **1**, 16119.

23 J. Li, K. McColl, X. Lu, S. Sathasivam, H. Dong, L. Kang, Z. Li, S. Zhao, A. G. Kafizas, R. Wang, D. J. L. Brett, P. R. Shearing, F. Corà, G. He, C. J. Carmalt and I. P. Parkin, *Adv. Energy Mater.*, 2020, **10**, 2000058.

24 S. Liu, H. Zhu, B. Zhang, G. Li, H. Zhu, Y. Ren, H. Geng, Y. Yang, Q. Liu and C. C. Li, *Adv. Mater.*, 2020, **32**, e2001113.

25 J. Ding, Z. Du, B. Li, L. Wang, S. Wang, Y. Gong and S. Yang, *Adv. Mater.*, 2019, **31**, 1904369.

26 X. Wang, Y. Li, S. Wang, F. Zhou, P. Das, C. Sun, S. Zheng and Z. S. Wu, *Adv. Energy Mater.*, 2020, **10**, 2000081.

27 S. Wei, C. Wang, S. Chen, P. Zhang, K. Zhu, C. Wu, P. Song, W. Wen and L. Song, *Adv. Energy Mater.*, 2020, **10**.

28 M. Harada, M. Kuwa, R. Sato, T. Teranishi, M. Takahashi and S. Maenosono, *ACS Appl. Nano Mater.*, 2020, **3**, 8389-8402.

29 F. Carraro, O. Vozniuk, L. Calvillo, L. Nodari, C. La Fontaine, F. Cavani and S. Agnoli, *J. Mater. Chem. A*, 2017, **5**, 20808-20817.